AGU PUBLICATIONS

JGR

Journal of Geophysical Research: Oceans

RESEARCH ARTICLE

10.1002/2014JC010020

**Key Points:**
- The barotropic flow makes an important contribution to mean zonal transport
- Vertical shear of the ACC varies in response to changes in topography
- The rotation in the velocity with depth produces across-stream transport

**Correspondence to:**
B. Peña-Molino,
beatriz.penamolino@utas.edu.au

**Citation:**
Peña-Molino, B., S. R. Rintoul, and M. R. Mazloff (2014), Barotropic and baroclinic contributions to along-stream and across-stream transport in the Antarctic Circumpolar Current, *J. Geophys. Res. Oceans*, *119*, 8011–8028, doi:10.1002/2014JC010020.

Received 4 APR 2014
Accepted 27 OCT 2014
Accepted article online 31 OCT 2014
Published online 25 NOV 2014

# Barotropic and baroclinic contributions to along-stream and across-stream transport in the Antarctic Circumpolar Current

**B. Peña-Molino[1], S. R. Rintoul[1,2,3], and M. R. Mazloff[4]**

[1]Antarctic Climate and Ecosystem Cooperative Research Centre, University of Tasmania, Hobart, Tasmania, Australia, [2]CSIRO Oceans and Atmosphere Flagship, Hobart, Tasmania, Australia, [3]Centre for Weather and Climate Research, A Partnership of CSIRO and the Australian Bureau of Meteorology, Hobart, Tasmania, Australia, [4]Scripps Institution of Oceanography, La Jolla, California, USA

**Abstract** The Southern Ocean's ability to store and transport heat and tracers as well as to dissipate momentum and energy are intimately related to the vertical structure of the Antarctic Circumpolar Current (ACC). Here the partition between barotropic and baroclinic flow in the time-mean ACC is investigated in a Southern Ocean state estimate. The zonal geostrophic transport is predominantly baroclinic, with at most 25% of the transport at any longitude carried by the barotropic component. Following surface streamlines, changes in vertical shear and near-bottom velocity are large, and result in changes in the local partition of barotropic/baroclinic vertically integrated transport from 10/90% in the center of the basins, to 50/50% near complex topography. The velocity at depth is not aligned with the surface velocity. This nonequivalent barotropic flow supports significant cross-stream transports. Barotropic and baroclinic mass transport across the ACC is, on average, in opposite directions, with the net barotropic cross-stream transport being poleward and the net baroclinic equatorward. The sum partially cancels out, leaving a net geostrophic poleward transport across the different fronts between −5 and −20 Sv. Temperature is also transported across the fronts by the nonequivalent barotropic part of the ACC, with maximum values across the northern ACC fronts equivalent to −0.2 PW. The sign and magnitude of these transports are not sensitive to the choice of stream-coordinate. These cross-stream volume and temperature transports are variable in space, and dependent on the interactions between deep flow and bathymetry, thus difficult to infer from surface and hydrographic observations alone.

## 1. Introduction

The Southern Ocean's (SO) ability to store and transport heat as well as other tracers relies both on the horizontal circulation of the Antarctic Circumpolar Current (ACC) and the overturning circulation coupled to it. The structure of these circulations influences the ACC's sensitivity to a changing climate and as such has been the subject of an increasing number of studies. Here we investigate how the vertical structure shapes the transport of the time-mean ACC, characterize its spatial variability, and evaluate the impact it has on the "permeability" of the current.

It is a common practice in the study of geophysical flows to characterize their vertical structure by separating the flow into a depth-independent component, typically referred to as barotropic, and depth-dependent component, referred to as baroclinic. There are a number of different ways to do such separation. In theoretical as well as modeling studies, the usual approach is to consider the depth-independent flow as the depth-averaged flow, $\bar{u}$, and the departure from the vertical average, $u'$, as the depth-dependent component. Another such approach extensively used by the observational community, and the one adopted here, is to separate the flow into a depth-independent component equal to the geostrophic flow at the bottom, $u_{bottom}$, and a depth-dependent component, $u_{rel}$, equal to the geostrophic flow referenced to zero at the bottom. The latter, $u_{rel}$, can be inferred from hydrographic observations alone, as it is in balance with horizontal gradients in the density field. Through the efforts of the World Ocean Circulation Experiment (WOCE), this part of the transport has been well documented across the three major chokepoints in the ACC: at Drake Passage across the WOCE Southern Repeat section 1 (SR1) where the baroclinic transport is 136.7 ± 7.8 Sv [*Cunningham et al.*, 2003], south of Australia across WOCE section SR3 with 147 ± 10 Sv [*Rintoul and Sokolov*, 2001], and south of Africa across WOCE section SR2 with baroclinic

transport of 145 $\pm$ 3.9 Sv [*Swart et al*., 2008]. The geostrophic flow at the bottom, on the other hand, is hard to measure and remains mostly unknown.

Observations show the ACC consists of a number of fronts, of which the Subantarctic (SAF) and Polar Fronts (PF) are the main ones. These fronts separate waters with different characteristics and can be identified by their hydrographic properties along the circumpolar path of the current [*Orsi et al*., 1995]. They are aligned with deep reaching jets, and despite the somewhat discontinuous nature of the jets, often merging and splitting, they tend to be associated with particular SSH values and are in this sense circumpolar in nature [*Sokolov and Rintoul*, 2007, 2009]. Interestingly, these deep reaching jets can both inhibit motion across the fronts at some locations and promote strong cross-front exchange in other locations [*Ferrari and Nikurashin*, 2010; *Naveira Garabato et al*., 2011; *Thompson and Sallée*, 2012].

Our current view of the ACC vertical structure derives from the early observation by *Killworth* [1992] that the streamlines in the Fine Resolution Antarctic Model were self-similar with depth, in other words, parallel and proportional to the surface streamlines. Killworth's work motivated a series of analytical models for an *equivalent barotropic* (EB) ACC, as the term was coined [*Marshall et al*., 1993; *Krupitsky et al*., 1996; *Ivchenko et al*., 1999]. To obtain closed form solutions, these studies required variations in topography to be small.

Numerous studies have assumed an EB structure and represented the ACC as an exponentially decaying jet [*Gille*, 2003; *Karsten and Marshall*, 2002; *Hughes*, 2005]. However, the requirement that variations in topography be small is not always met along the ACC. Furthermore, the presence of large topographical obstacles along the ACC plays a fundamental role in shaping its horizontal structure, by steering of the current [e.g., *Marshall*, 1995; *Hughes et al*., 1999; *Moore et al*., 1999] and by regulating the branching and merging of the individual jets in the ACC [*Thompson*, 2010]. However, the degree to which the ACC path is locked to the bathymetry depends on the vertical structure of the current itself. In the absence of baroclinicity, the flow must follow $f/h$ contours resulting in very low circumpolar transport. In the real ocean, the presence of stratification allows the flow to decouple from the bottom [*Olbers and Eden*, 2003]. Thus both stratification and topography are required to produce a realistic ACC.

The ACC vertical structure and its interactions with topography have profound implications for the dynamical balances. The momentum input by the wind in the ACC is balanced by the form drag induced by large topographic obstacles along the ACC's path [e.g., *Munk and Palmén*, 1951; *Gille*, 1997]. The barotropic and baroclinic components of the pressure field, however, play rather different roles in this balance; while the baroclinic bottom pressure acts to accelerate the eastward flow in the ACC, the barotropic bottom pressure removes momentum from it [*Olbers et al*., 2004]. Bottom pressure gradients play an equally important role in the integrated vorticity balance, where bottom pressure torque is a dominant term [*Hughes*, 2005]. The EB model for the ACC proposed by *Killworth and Hughes* [2002] does not contain the large-scale balance between bottom pressure torque and wind stress curl in the integrated vorticity budget, suggesting some important dynamics are missed; the assumptions of weak bottom flow and small variations in depth likely break down in the vicinity of topography. In addition, large bottom velocities over rough topography ($>$10 cm s$^{-1}$) are essential to maintain the abyssal internal wave field required to dissipate energy in the ACC [*Nikurashin and Ferrari*, 2011]. Such large bottom velocities are not properly represented in EB models with rapidly decaying velocity profiles [*Hughes*, 2005; *Killworth and Hughes*, 2002].

Knowledge of the vertical structure of the ACC is needed to reconstruct full water column properties from vertically integrated or surface measurements as in the Gravest Empirical Mode approach [*Sun and Watts*, 2001; *Meijers et al*., 2011]. The skill of such a reconstruction depends on the degree to which each value of the integral property (e.g., SSH or acoustic travel time) corresponds to a single vertical profile. However, knowledge of the contribution of the barotropic flow is still lacking. The few available observations, usually point measurements, of the partition between barotropic and baroclinic flow often disagree on whether geostrophic velocity calculations referenced to zero at the bottom accurately predict the transport of the ACC, overestimate it, or underestimate it [*Donohue et al*., 2001], reflecting the spatial variability in the partition between baroclinic and barotropic motions. In addition, observations of the near-bottom pressure field in the SAF south of Australia [*Tracey et al*., 2006] as well as at Drake Passage [*Chereskin et al*., 2009] revealed a vigorous deep velocity field that is not aligned with the flow at the surface.

In this study, we explore the nature of barotropic and baroclinic motions in the ACC based on a dynamically consistent state estimate that incorporates the available observations in the Southern Ocean. The details of

the model are discussed in section 2, along with definitions of the along-stream and across-stream reference frame used in the following sections. In section 3, we evaluate the contribution of barotropic and baroclinic flow to the vertically integrated zonal transport. In section 4, we examine the partition between baroclinic and barotropic flow in the along-stream direction and how changes in vertical shear contribute to this partition. In section 5, we look at rotation of the flow with depth and estimate the volume and temperature cross-stream transports that occur in the time-mean ACC due to this rotation. Section 6 presents the discussion and section 7 summarizes our main conclusions.

## 2. Methods

### 2.1. The Southern Ocean State Estimate

The Southern Ocean State Estimate (SOSE) is based on the MITgcm [*Marshall et al*., 1997]. It is eddy permitting at 1/6° horizontal resolution and has 42 vertical levels of varying depth. The model assimilates a large number of observations (including Argo, altimetry, CTD, and XBT data) using the adjoint method to carry out successive adjustments to the initial and meteorological conditions that bring the model closer to the observations. As such, the model has undisturbed physics while fitting the modern observations better than available climatologies [*Mazloff et al*., 2010]. Topography is represented by means of partial cells, which partially mitigates some of the problems with classic step-like representations of the bottom [*Adcroft et al*., 1997], making the model more adequate to explore near-bottom dynamics.

SOSE does not assimilate velocities, however, comparison with an independent ADCP record at Drake Passage showed good agreement on the structure and amplitude of the ACC [*Firing et al*., 2011]. Changes in the vertical structure of the flow upstream of Macquarie Ridge and at the ridge itself are also well represented in SOSE's velocity field [*Rintoul et al*., 2014]. Our analysis makes use of geostrophic velocities derived from the model's pressure potential anomaly field, diagnosed by solving a two-dimensional elliptical problem that guarantees nondivergence of the modeled total velocities [*Marshall et al*., 1997]. Modeled velocities are nearly in geostrophic balance, except for near the surface where large differences between the calculated geostrophic velocities and the modeled velocities occur due to Ekman flow. Geostrophic velocities calculated from the pressure field are well behaved (slowly varying) within the deepest layers and do not suffer from potential problems associated with the unresolved bottom boundary layer. Zonal geostrophic transports for the typically monitored sections across the ACC are presented in section 3. For a more detailed comparison of the model to observations as well as other model specifications, the reader is referred to *Mazloff et al*. [2010].

SOSE's output is available for the period 2005–2010. Further adjustments between model and observations are continuously underway. The work presented here is based on the 6-year mean fields for the entire assimilation period, available at sose.ucsd.edu.

### 2.2. The Streamline Reference Frame

Along its path the ACC experiences large departures from zonal flow at several locations. These north-south excursions play an important role in the meridional overturning and dynamics of the ACC [*Dufour et al*., 2012; *Zika et al*., 2013; *Mazloff et al*., 2013]. As we seek to distinguish along-stream and across-stream transports, we use a streamwise reference frame. In a flow that rotates with depth, there is no single choice of streamwise coordinate that follows the flow direction at all depths, and therefore all stream-coordinate definitions are an approximation. Numerous definitions have been used in the literature. Here we are interested in characterizing the spatial variability in the partition between depth-dependent and depth-independent transport for both the part of the ACC that behaves in an EB way, and for the part of the flow whose direction changes with depth (Figure 1). As reconstructions of the three-dimensional structure of the ACC based on the EB model are often mapped along dynamic height contours, we use a coordinate system defined by sea surface height (SSH) streamlines. This coordinate system is used in section 4 to examine the spatial variability in the vertical shear of the horizontal velocity as well as in section 5, where we quantify the degree of turning of the horizontal velocity with depth.

In section 5.1, we evaluate volume and temperature transport across the time-mean northern, center, and southern branches of the Subantarctic Front (SAF-n, SAF-c, and SAF-s), the northern and southern branches of the Polar Front (PF-n and PF-s), and across the Southern ACC front (SACCF). Streamlines corresponding to

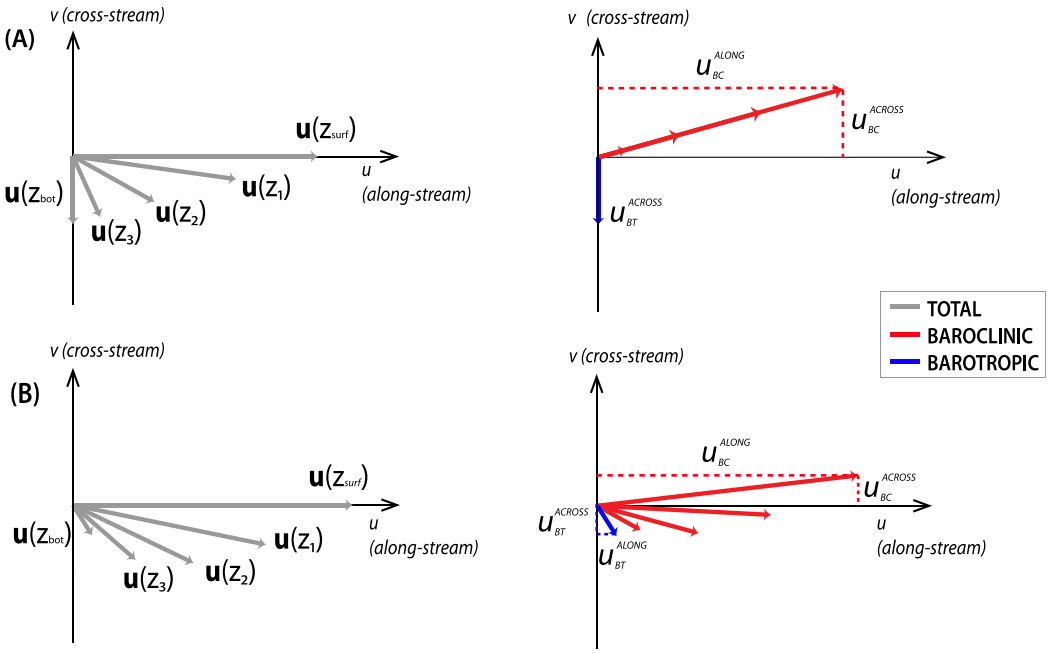


**Figure 1.** Schematic depicting two idealized velocity profiles for flows that rotate clockwise with increasing depth. For simplicity, the along-stream direction, here given by the direction of the surface flow ($\mathbf{u}(z_{surf})$), is chosen to be zonal. In case (a), there is no rotation in the baroclinic flow (red), and rotation of the total velocity vector (gray) is only due to the barotropic component (blue) being at an angle with the surface flow. In case (b), rotation in the total flow results from both the barotropic component as well as rotation in the baroclinic component. The dashed lines show in red the along-stream and across-stream baroclinic velocity at the surface ($u_{BC}^{ALONG}$ and $u_{BC}^{ACROSS}$, respectively), and the along-stream and across-stream barotropic velocity in blue ($u_{BT}^{ALONG}$ and $u_{BT}^{ACROSS}$). By construction $u_{BC}^{ACROSS}$ at the surface and $u_{BT}^{ACROSS}$ have equal magnitude and opposite direction. The along-stream barotropic component in case (a) is zero.

the fronts are obtained by selecting the time-mean SSH contours within the T/S range of each front as per their classical definitions [*Orsi et al*., 1995; *Sokolov and Rintoul*, 2007] that are associated with the largest surface speed averaged over the entire T/S defined streamline. Circumpolar integrals along the fronts are carried out along discrete versions of the streamlines that follow the model grid cell faces, to ensure there is no accumulation of interpolation errors. The cross-stream transports by the mean flow estimated here are different from those obtained by time averaging the instantaneous transports across the time-varying front locations due to the time-varying cross-stream velocities. As changes in front positions can be significant at times, and transient velocities are large along the instantaneous path of the fronts, a large eddy component of the mean cross-stream transport could exist; this eddy component is not represented in our analysis.

The northern and southern boundaries of the circumpolar ACC are simply defined by the northernmost and southernmost SSH contours that pass through Drake Passage. In section 3, contours of vertically and meridionally integrated zonal geostrophic transport are used to define the ACC envelope.

The results presented here are not sensitive to the choice of streamlines. Repeating the analysis using time-mean vertically integrated transport streamlines gave similar results for vertical shear and total cross-stream transport of mass and temperature, albeit with minor differences, as the streamline integrals depend on the exact path of integration. The partitioning of the cross-stream transport between the barotropic and baroclinic components, on the other hand, does depend on the choice of streamlines. When calculated along transport streamlines, a more even partitioning is found, since in a flow that turns with depth the vertically averaged flow is at an angle to both the surface and near-bottom flow.

At depth, fronts follow more closely the direction of vertical shear which is, by thermal wind, tangent to isopycnals on a pressure surface. As such vertical shear is often used as reference frame in observational studies based on moored measurements [*Phillips and Rintoul*, 2000; *Sekma et al*., 2013]. However, the direction of the cross-stream velocity in this reference frame varies with depth, making the integral of cross-stream transports along streamlines much more complex [*Viebahn and Eden*, 2012]. In SOSE, the direction of the vertical shear also varies with depth, but in general remains within 20° of the direction of the SSH streamlines. Differences in local estimates of cross-stream transport using shear and SSH streamline coordinate

systems are small, but must be taken into account when comparing our circumpolar integrals with circumpolar extrapolations of point measurements in shear coordinates.

## 3. The Zonal Geostrophic Transport in SOSE

The total zonal geostrophic transport can be separated into a contribution from the near-bottom velocity, or barotropic transport $U_{BT}$, and a contribution from the velocity relative to the bottom, or baroclinic transport $U_{BC}$, which represents the contribution from the vertical shear associated with the density field. Observations of the baroclinic component of the transport are much more abundant as they are obtained from the density field, which is readily observed. Observations of the barotropic transport on the other hand are more scarce. They can be obtained in two ways: by measuring directly the velocity at a reference level, in which case transients and nongeostrophically balanced motions can significantly contribute to the measured value, or alternatively by measuring the bottom pressure field at sufficient spatial resolution and using geostrophy to derive near-bottom velocity. Although both these types of observations are becoming more available, they are still insufficient to explore the spatial variability of the partition between barotropic and baroclinic flow.

SOSE's geostrophic velocities, unlike hydrography-based calculations, are derived from the model's pressure field, and include the reference level contribution. Near-bottom geostrophic velocities from SOSE's mean field are typically smaller than 1 cm $s^{-1}$ in the center of the basins, in good agreement with the circumpolar average estimated by *Gille* [2003] of 0.4 cm $s^{-1}$. Around large topographic obstacles SOSE's near-bottom velocities increase to 5 cm $s^{-1}$, compared to values of 3.6–5.9 cm $s^{-1}$ measured downstream of the Southeast Indian Ridge [*Phillips and Rintoul*, 2002]. Values in excess of 10 cm $s^{-1}$ are found in the deep passages across the ridges, such as the main gap through Macquarie Ridge and Fawn Trough, as well as along the continental slope in Drake Passage. These higher values also compare well with observations [*Chereskin et al*., 2009; *Ferrari et al*., 2012; *Sekma et al*., 2013; *Rintoul et al*., 2014]. These model-to-observation comparisons, despite the good agreement, provide a very limited basis to assess the accuracy of the model's near-bottom velocities. However, assimilation of hydrographic observations via the adjoint method has been shown to significantly improve the modeled deep circulation, even when the observations are limited to the upper 1000–2000 m of the water column [*Forget et al*., 2008].

The meridional integral of the zonal baroclinic and barotropic transport provides an approximate picture of the circulations associated with each component (top and middle plots of Figure 2). The total geostrophic transport is predominantly baroclinic, thus baroclinic transport contours largely resemble total transport streamlines [see *Mazloff et al*., 2010, Figure 7]. Despite the larger magnitude of the baroclinic transport, barotropic transports are not negligible. Across the three major choke points, the mean geostrophic barotropic (baroclinic) transport is 28 (121) Sv at Drake Passage (SR1), −28 (183) Sv south of Africa (SR2), and 16 (149) south of Australia (SR3; bottom plots of Figure 2). The barotropic transport at SR2 and SR3 is carried by the near-bottom flow outside the ACC envelope, where different dynamics apply. However, the barotropic transport is often large within the circumpolar band of the ACC. Integrating the transport in the circumpolar band alone (Figure 3), we find that on average 15% of the zonal transport is carried by the near-bottom flow, with values exceeding 20% found upstream and downstream from Kerguelen Plateau, at Drake Passage, and over the Macquarie, Mid-Pacific, and Mid-Atlantic Ridges. In the center of the basins, near-bottom zonal velocities often change sign across the ACC latitude range (not shown here), possibly indicating the presence of deep recirculation gyres [*Nadeau and Straub*, 2012]. Integrated meridionally they cancel out, producing a very small contribution to the total transport.

## 4. The Role of Vertical Shear and Bottom Velocity in the Along-Stream Flow

Next, we consider the spatial distribution of the baroclinic and barotropic contribution to the along-stream vertically integrated transport. We find that over large areas of the circumpolar ACC more than 90% of the vertically integrated transport in the along-stream direction is carried by the baroclinic component (values $<$10% in Figure 4). However, there is a lot of small-scale structure, some of which is associated with the transitions between fronts and frontal zones, and indicates that even in the mean the flow has a very filamented nature. Other small-scales features are likely to be stationary meanders whose signature may be eliminated by longer time averaging. There are several large areas over which the barotropic vertically integrated

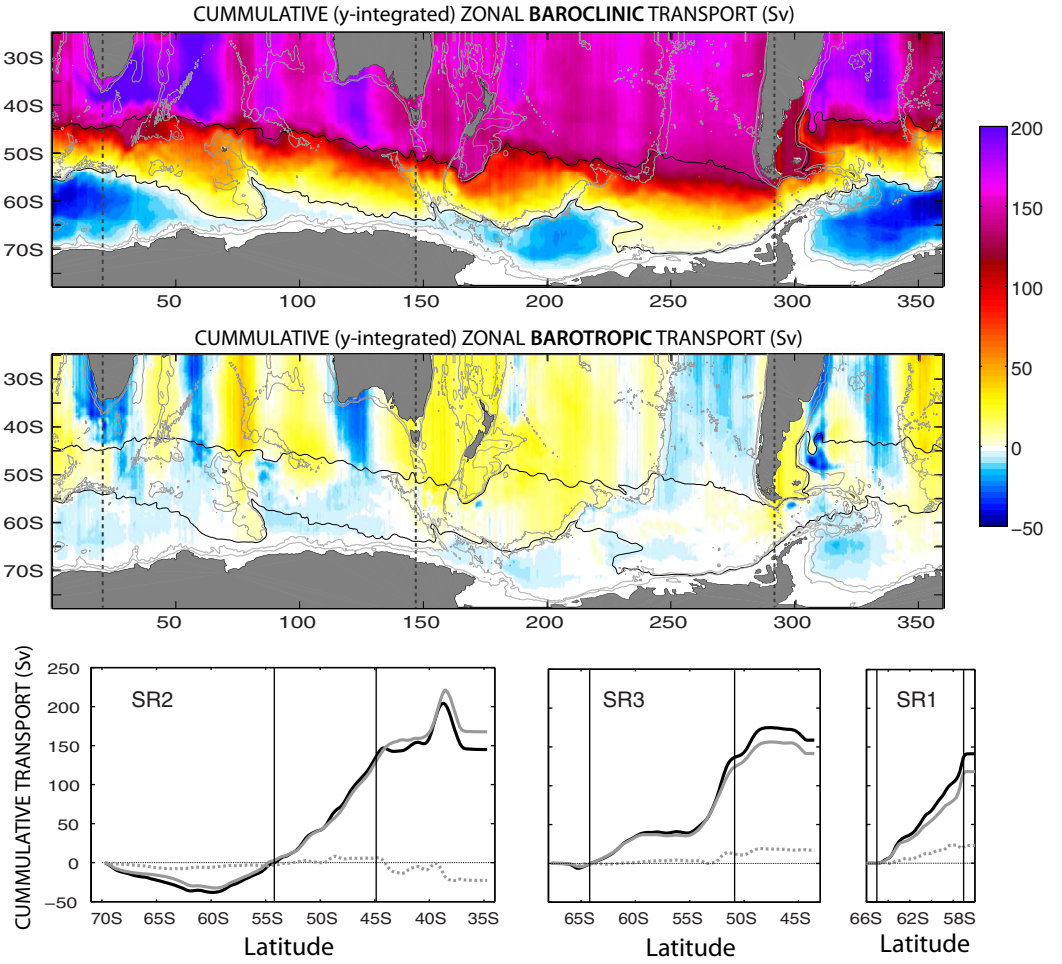


**Figure 2.** Cumulative zonal (top) baroclinic transport and (middle) barotropic transport. The thick black contours indicate the location of the 0.5 and 142 Sv geostrophic transport contours. The 100, 1000, and 3000 m isobaths are indicated by the thin gray contours. The bottom plots show sections of baroclinic transport (solid gray), barotropic transport (dashed gray), and the sum (solid black) extracted at the three major chokepoints, south of Africa, SR2, south of Australia, SR3, and at Drake Passage, SR1. All transports shown here are meridionally integrated; zonal transports between two given latitudes can be recovered by taking the meridional derivative.

transport is enhanced and carries over 50% of the local transport. Northeast of Kerguelen Plateau, between the Southeast Indian and Macquarie Ridge, and along the Malvinas current are regions where strong barotropic flows significantly contribute to the total transport of the ACC. At other locations, such as east of Campbell Plateau, in the southeast Pacific Sector, and east of the Malvinas Current, the barotropic component accounts for a large fraction of the transport, but the mean flow is weak in these regions and so the barotropic flow makes a small contribution to the total transport across the ACC.

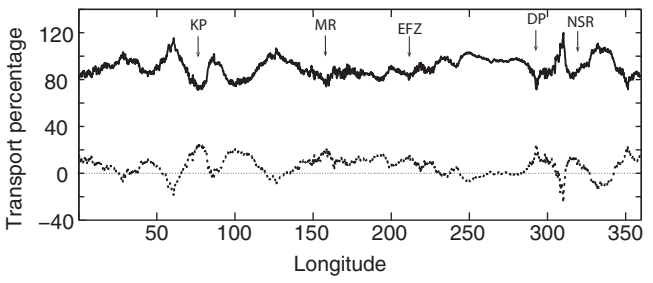


**Figure 3.** Percentage of the zonal transport integrated between the 0.5 and 142 Sv geostrophic transport contours carried by the baroclinic component (solid) and by the barotropic component (dashed). Arrows indicate the approximate positions of Kerguelen Plateau (KP), Macquarie Ridge (MR), Eltanin Fracture Zone (EFZ), Drake Passage (DP), and North-Scotia Ridge (NSR).

Estimates of the ratio between barotropic and baroclinic transport from observations suggest spatial variability like that shown in Figure 4 occurs in the real ocean [e.g., *Phillips and Rintoul*, 2002; *Cunningham et al.*, 2003; *Smith et al.*, 2010]. Changes in this ratio are usually attributed to

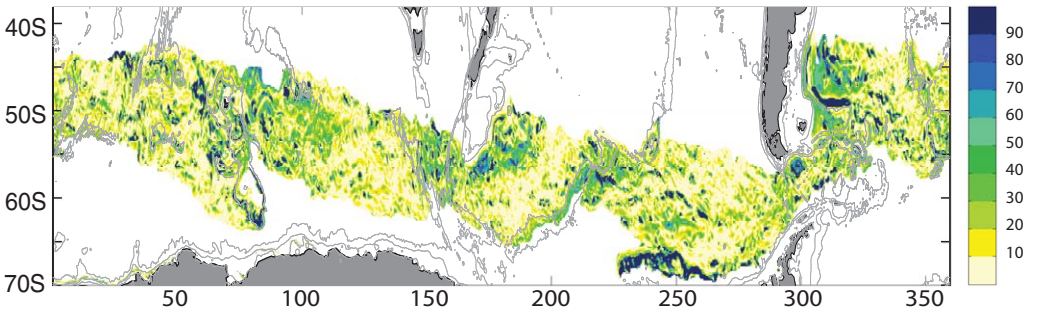


**Figure 4.** Percentage of the vertically integrated flow due to the barotropic component. The 100, 1000, and 3000 m isobaths are indicated by the thin gray contours.

changes in the amplitude of the near-bottom velocity. However, variability in the percentage of barotropic transport can also occur with little change to the near-bottom flow, but instead as a result of changes in the amplitude of the baroclinic flow alone. Past studies have often represented the vertically variable part of the ACC with a single function of depth, hence severely limiting the spatial variability in the baroclinic flow. However, stratification is not constant along streamlines, and rapid changes in depth can modify the modal composition of the flow, both by increasing the contribution of higher baroclinic modes as well as introducing bottom intensified modes [*Rhines*, 1970]. Thus, changes in the vertical structure of the flow along streamlines are likely to occur. We now analyze vertical shear to characterize the spatial variability in the baroclinic flow and assess the ability of a spatially constant EB structure to represent this variability.

To characterize the spatial distribution of vertical shear, we compute vertically averaged shear (the difference between surface and bottom flow divided by water depth) for the time-mean along-stream component of the geostrophic velocity at each grid point (Figure 5). To highlight changes the flow experiences as it navigates the topography, vertical shear values are mapped onto surface streamlines (SSH contours) every 0.05 m between the northern-most and southern-most circumpolar SSH streamlines. Then the streamline mean, positive for a flow with decreasing amplitude with increasing depth, is removed to produce vertical shear anomalies. Thus areas where the shear is larger than the streamline mean will appear as positive anomalies, whereas areas of negative anomalies correspond to regions where the shear is reduced compared to the streamline mean.

The relationship between shear and topography is clear from the vertically averaged shear anomalies (top plot of Figure 5): shear is reduced over the abyssal plains and enhanced in areas of complex topography. This topographic enhancement results from both vertical compression of the flow as well as increased surface velocity, and it can be better seen by considering vertical profiles of shear anomalies (relative to the streamline mean profile) rather than vertical averages. Examples along the SAF-n, PF-n, and SACCF are shown in Figure 5 (bottom plots).

Shear anomalies are in general single-signed throughout the water column. Maximum values are found within the top 750 m in the SAF and progressively shoal toward the south to depths of less than 200 m in the SACCF. Below the maxima, shear decreases with depth more rapidly in the upper ocean. Near-bottom shear anomalies tend to be small, with the exception of the Malvinas Current and the branch of the Southern ACC Front (SACCF) that flows through Fawn Trough [*Park et al.*, 2009; *Roquet et al.*, 2009]. At these locations shear anomalies remain large throughout the water column as the flow is vertically compressed by the shallower bathymetry. This vertical compression occurs along the strongest northward flows in the ACC, as expected from potential vorticity constraints.

However, the relationship between enhanced shear and shoaling bottom seen in the Malvinas Current and Fawn Trough cannot be extended to the rest of the domain. Although more apparent along the SACCF, this relationship does not hold in a circumpolar sense.

Enhanced surface velocities also contribute to large vertical shear. Surface velocities are often large where the ocean floor shoals, in part as a consequence of mass conservation. The Eltanin Fracture zone and Drake Passage are examples of this. At both these locations, the ACC is constricted meridionally as well as

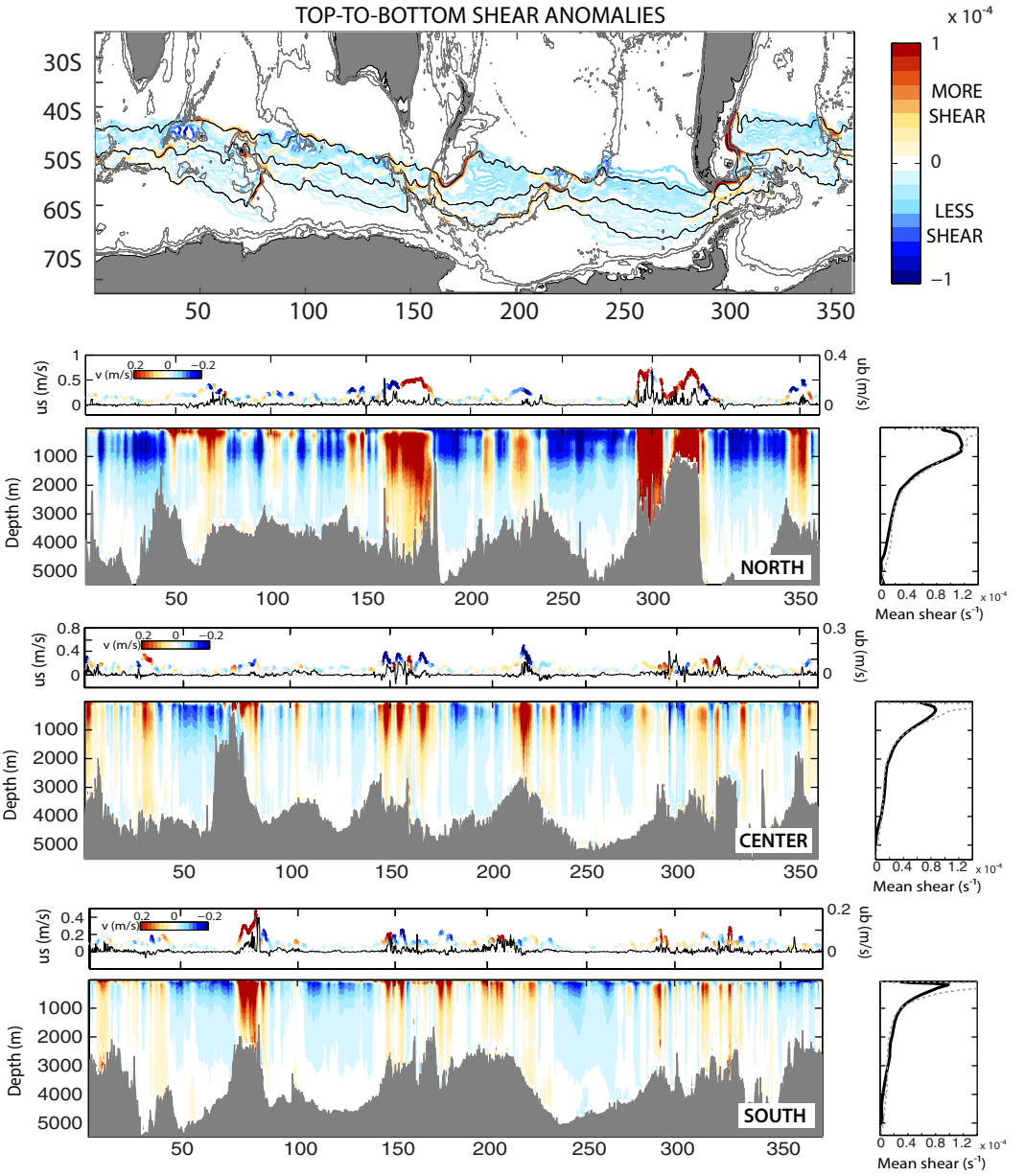


**Figure 5.** (top) Vertically averaged velocity shear anomalies along SSH contours. Anomalies are defined with respect to the streamline mean. Values range from $[-1, 1] \times 10^{-4}$ s$^{-1}$ color scale on the right. Positive indicates areas with enhanced shear, negative areas of reduced shear. SSH contours corresponding to the SAF-n (north), the PF-n (center), and the SACCF (south) are shown in black. Bathymetry (100, 1000, and 3000 m isobaths) is shown in gray. Full-depth shear anomalies (same range as above) for these three fronts are shown in the sections labeled as north, center, and south. The horizontal axis is distance along the streamline and has labels with the corresponding longitudes, hence the uneven spacing. The mean shear profile (solid black) and mean stratification (dashed gray) for the streamline are shown on the right of each section. Mean stratification profiles are normalized (no units) and scaled to match the amplitude of the mean shear. (left axis, color) Surface and (right axis) near-bottom along-stream velocity is shown on top of the sections. Additional information is provided by coloring the surface velocity according to the amplitude of the meridional velocity at the surface, $v_s$ (inset color scale).

compressed vertically, making mass conservation arguments even more compelling. However, enhanced surface velocities also are found downstream of many ridges and other large topographic obstacles, where the ocean deepens.

The component of the shear that is shaped by changes in surface velocity can be readily represented in simple EB models of the ACC, for example, through the spatially variable amplitude in an exponential function. However, a fixed vertical profile that does not account for cross-stream variations in the vertical scale of the

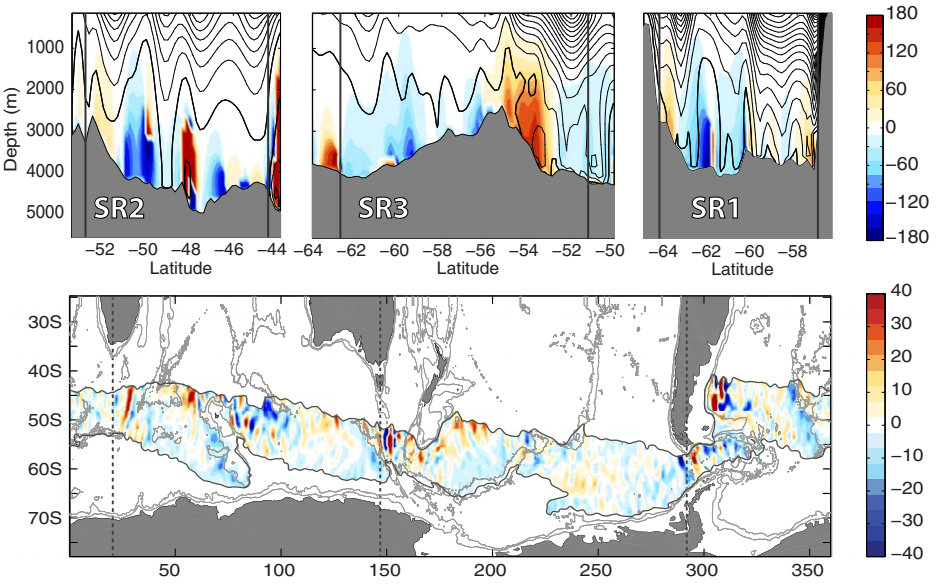


**Figure 6.** (top) Rotation of the geostrophic velocity vector, in degrees, for the SR2, SR3, and SR1 sections. Negative values indicate clockwise rotation with increasing depth, positive indicate counterclockwise. The location of the northernmost and southernmost circumpolar SSH contours is shown by the vertical lines. Black contours represent mean speed ($(u^2+v^2)^{1/2}$) at 0.02 m $s^{-1}$ intervals, with the thickest contour indicating the 0.02 m $s^{-1}$. (bottom) Vertically integrated cross-stream transport or transport per unit length ($m^2$ $s^{-1}$) for the circumpolar ACC. Positive values correspond to counterclockwise rotation and indicate equatorward transports. Negative transports are poleward and correspond to clockwise rotation. The location of the sections above is shown by the dashed lines, and the 100, 1000, and 3000 m isobaths are shown in gray.

current and reduced shear in areas of enhanced near-bottom flows, will fail to characterize much of the spatial variability of the vertical structure of the ACC.

## 5. The Rotation of the Horizontal Velocity With Depth

Models often show the vertical structure of the ACC is close to equivalent barotropic [*Killworth*, 1992; *Killworth and Hughes*, 2002]. More recently, direct velocity observations at Drake Passage have also shown that the ACC is self-similar with depth in the upper 1000 m (although the vertical structure varies with location) [*Firing et al*., 2011]. However, this may not be the case at greater depths. Near-bottom zonal velocities inferred from hydrographic observations referenced to surface [*Donohue et al*., 2001] and middepth [*Gille*, 2003] velocity observations are sometimes westward in areas where the baroclinic transport is eastward, suggesting some degree of rotation with depth exists. In fact, direct observations of near-bottom velocities show that in certain areas the direction of the surface and bottom flows in the ACC can be quite different [*Tracey et al*., 2006; *Chereskin et al*., 2009]. Quantifying changes in flow direction with depth and separating contributions to rotation from the barotropic and baroclinic components is the aim of this section.

We compute the direction of the velocity vector relative to the surface flow at each depth for the circumpolar envelope of the time-mean ACC. Negative angles indicate clockwise rotation and positive values indicate counterclockwise rotation. A value of zero corresponds to the case of flow at depth parallel to the surface flow. Three sections across the time-mean ACC at the main choke points are shown in Figure 6: south of Africa where the circumpolar ACC flows through relatively unobstructed terrain (SR2), south of Australia across the Southeast Indian Ridge (SR3), and at Drake Passage (SR1). In all three cases, rotation increases with depth but remains small within the jets down to 1000 m, and down to greater depths in areas where the jets are deep reaching. At SR1, where the jets penetrate further down, the angles are generally smaller. Rotation tends to be larger in the jet flanks where the mean currents are generally weak. Alternating patches of positive and negative values are found in all three sections. Areas where values reach $\pm 180^\circ$ near the bottom are mostly seen at SR2 and SR3. The horizontal scale of these patches, O(100)km, approximately matches the scales over which changes in bathymetry occur. Vertical velocity at the bottom (not shown) shows this pattern of rotation is in fact connected to topographically induced upwelling/

downwelling. In areas where the bottom rises (deepens), the velocity vector turns clockwise (counterclockwise) with increasing depth, and positive (negative) vertical velocities occur. This relationship between the turning of the horizontal velocity with depth and vertical velocity, first used by *Bryden* [1976] to estimate vertical velocity from a line of current meters in the Gulf Stream, and later exploited by others in the ACC [*Phillips and Rintoul*, 2000; *Tracey et al*., 2006] in the context of meanders, holds here too for topographically induced vertical velocity.

Naturally these areas where rotation is high and the along-stream velocity is low do not contribute much to the zonal transport. On average over the circumpolar ACC only 10% of the zonal transport is carried by the non-EB ACC flow, defined as areas with time-mean rotation exceeding $\pm 10^\circ$ (approximately given by the 2 cm $s^{-1}$ isotach, the deepest contour in Figure 6). However, high rotation areas are responsible for the cross-stream transport in the time-mean ACC. To quantify this cross-stream transport, we vertically integrate the component of the flow normal to the surface streamlines, and smooth the resulting field with a $2^\circ \times 2^\circ$ window to eliminate some of the small-scale structure and highlight large-scale changes. Transports per unit length of 20 $m^2$ $s^{-1}$ (equivalent to 2 Sv integrated over a length of 100 km) and higher are obtained this way through most of the circumpolar band (bottom plot of Figure 6). These transports can be characterized as either large areas (tens of degrees of longitude) of positive and negative rotation located in the center of the basins or small-scale bands (O(100)km)) in the vicinity of complex topography. The connection between these two rotation regimes and the baroclinic and barotropic components of the flow is explored in more detail next.

### 5.1. Implications for Cross-Stream Transport

For a purely EB baroclinic flow, both velocity and vertical shear are parallel at all depths and tangent to isopycnals on pressure surfaces. A barotropic component with a different direction can be added to this baroclinic flow without altering the vertical shear of the total (barotropic plus baroclinic) geostrophic flow. The addition of the barotropic component causes the total geostrophic velocity to gradually rotate with depth (Figure 1). Alternatively, rotation in the baroclinic component may occur when the direction of the vertical shear itself varies with depth. Next, we evaluate these two sources of rotation by vertically integrating both barotropic and baroclinic velocities normal to the surface streamlines. As before, cross-stream transports are smoothed over a $2^\circ \times 2^\circ$ window to highlight changes over larger scales.

Barotropic cross-stream transports are in general larger and spatially more variable than baroclinic transports (Figure 7). Values exceeding 20 $m^2$ $s^{-1}$ occur more often toward the northern part of the ACC. Patterns in total cross-stream transport are in general similar to barotropic cross-stream transports (Figure 6). Exceptions are found west of the Kerguelen Plateau and along the continental slope of the Campbell Plateau, where baroclinic cross-stream transports are larger and dominate the total.

At the small scales (O(100)km), the dominant features in the barotropic cross-stream transport are the narrow bands with alternating sign also seen in the total cross-stream transport. They are most clear between the Southeast Indian Ridge and Macquarie Ridge and along the northern edge of the Kerguelen Plateau, and correspond to areas with large stationary meanders. Rotation of the horizontal velocity with depth alternates sign as we move through crests and troughs as described by *Bryden* [1976].

At the basin scale, there is a tendency for the barotropic and baroclinic cross-stream transports to oppose each other. This is partly due to the fact that across SSH streamlines barotropic and baroclinic flow are exactly equal and opposite at the surface, and even in the absence of rotation in the baroclinic flow there is a baroclinic transport across SSH contours (see Figure 1). However, patterns in baroclinic cross-stream transport also reflect rotation in the baroclinic field. Rotation of the baroclinic flow, as shown by the angle between the baroclinic flow at the surface and at depth (Figure 8, top plots) increases away from the surface, but remains small in areas where the baroclinic flow exceeds 2 cm $s^{-1}$. The cross-front transport distribution that results from vertically integrating the component of the baroclinic flow that is normal to the baroclinic flow at the surface (bottom plot of Figure 8) is very similar to the distribution of cross-stream transport (top plot of Figure 7), but approximately 30% smaller in magnitude.

Patterns in baroclinic cross-front transport resemble large-scale changes in bathymetry. Poleward cross-front transport occurs in areas where the flow rotates clockwise with increasing depth; these areas tend to be located upstream from large topographic obstacles where the bottom rises following streamlines.

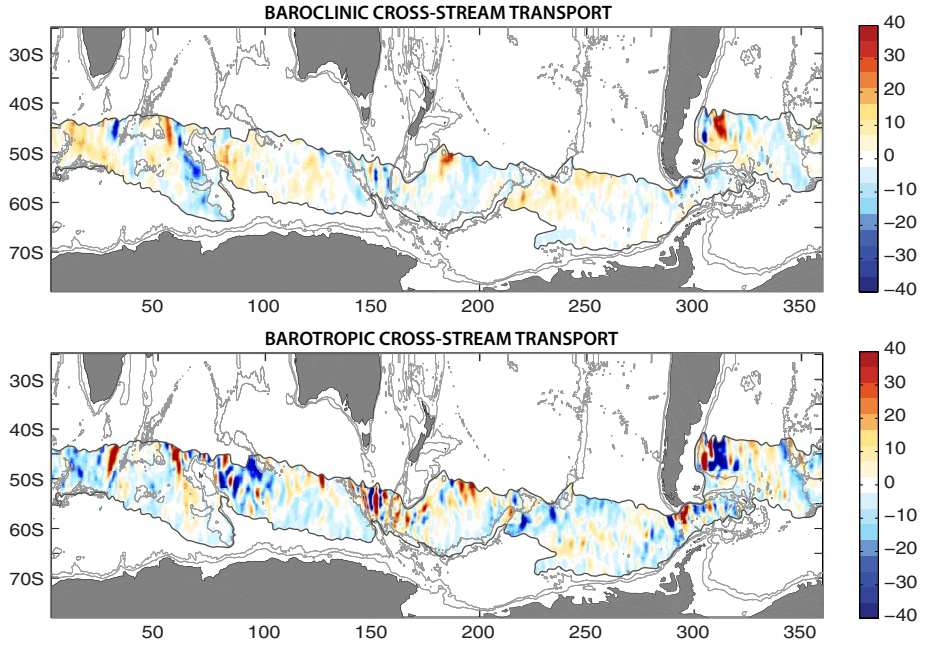


**Figure 7.** (top) Baroclinic and (bottom) barotropic cross-stream transport per unit length ($m^2\ s^{-1}$) for the circumpolar ACC. Positive values indicate equatorward transports, negative poleward. The northern and southernmost circumpolar SSH streamlines are shown by the black contours. Also shown (gray) are the 100, 1000, and 3000 m isobaths.

Equatorward transport, due to counterclockwise rotation, occurs in areas where the bottom deepens in the direction of the streamlines. Calculating the depth gradient along SSH streamlines clearly shows this relationship between turning in the baroclinic flow field and changes in depth along streamlines (compare Figures 8 and 9). However, rotation in the baroclinic flow, hence rotation in the density field itself, is associated only with gradual changes in depth in the center of the basins. The vertical stretching/squeezing and

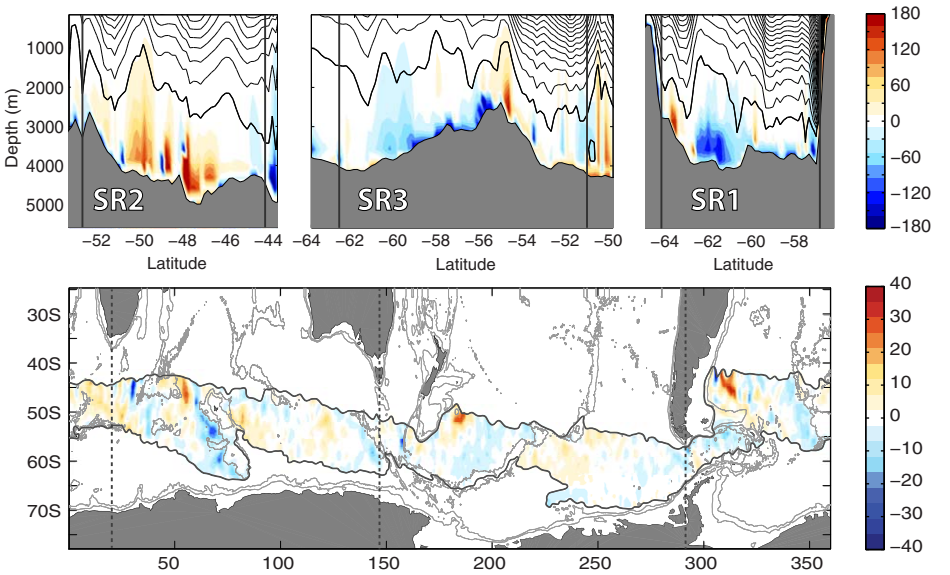


**Figure 8.** (top) Rotation, in degrees, of the baroclinic flow relative to the baroclinic flow at the surface across the SR2, SR3, and SR1 sections. Negative values indicate clockwise rotation with increasing depth, positive indicate counterclockwise. The location of the northernmost and southernmost circumpolar SSH contours is shown by the vertical lines. Black contours represent mean baroclinic speed ($((u^2+v^2)^{1/2}$) at 0.02 m $s^{-1}$ intervals, with the thickest contour indicating the 0.02 m $s^{-1}$. (bottom) Cross-front transport ($m^2\ s^{-1}$) calculated as the vertical integral of the baroclinic flow normal to the baroclinic flow at the surface. Positive values correspond to counterclockwise rotation and indicate equatorward transports. Negative transports are poleward and correspond to clockwise rotation. The location of the sections above is shown by the dashed lines, and the 100, 1000, and 3000 m isobaths are shown in gray.

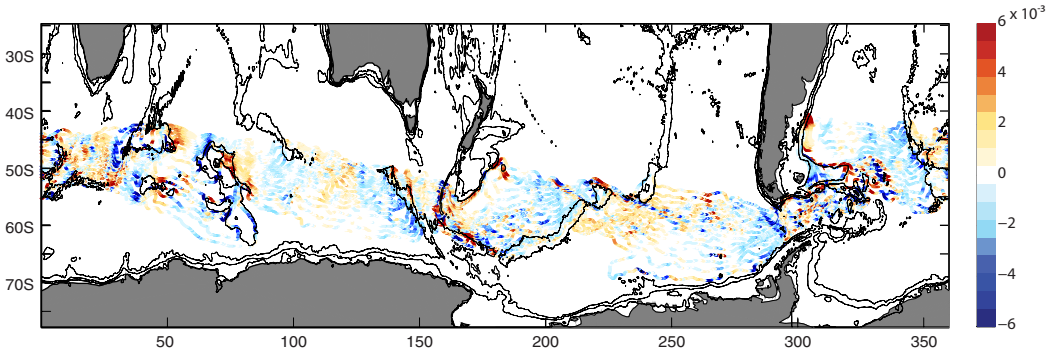


**Figure 9.** Depth gradient along SSH streamlines (dimensionless). Negative values indicate areas where the bottom shoals, and positive where it deepens. Values are shown for SSH streamlines every 0.05 m within the circumpolar range ([−1.1, 0.2] m). A smoothing window equivalent to 2° of longitude has been applied along the streamlines. Shown in black are the 100, 1000, and 3000 m isobaths.

resulting changes in potential vorticity induced by rapid changes in topography are more likely to destabilize the flow, hence the lack of turning in the baroclinic flow around sharp bathymetric features.

Baroclinic and barotropic cross-stream transports frequently change sign along the circumpolar ACC. Despite the variability in the direction of the cross-stream transport, both barotropic and baroclinic cross-stream transports are large when integrated along SSH streamlines:

$$V_{BT} = \int_s \int_{-h}^{0} \hat{v}_{bot} \mathrm{d}z\mathrm{d}s'$$

$$V_{BC} = \int_s \int_{-h}^{0} \hat{v}_{rel}(z) \mathrm{d}z\mathrm{d}s'$$

where $\hat{v}_{bot}$ and $\hat{v}_{rel}$ are the barotropic and baroclinic cross-stream velocity, and $s$ is given by the time-mean along-stream direction. Values for these integrals along the SAF-n,c,s, the PF-n,s, and the SACCF are shown in Figure 10. Baroclinic cross-stream transports are positive (equatorward) for all six frontal branches, with values ranging from 20 Sv in the PF-n and SAF-c to 50 Sv in the SAF-s. Barotropic transports are negative (poleward) with values for the different fronts spread over a wider range. Between 35 and 75 Sv move poleward across the different branches of the SAF, while the poleward transport ranges from 30 to 50 Sv across the PF and the SACCF. The small-scale features in the barotropic transport, earlier attributed to the presence of stationary meanders, are evident here too. Stationary meanders are most prominent on the northern edge of the Kerguelen Plateau and between the Southeast Indian Ridge and the Macquarie Ridge. In these regions, the barotropic transport becomes more negative in the SSH range of the SAF where the signal from the stationary meanders is the strongest.

Barotropic and baroclinic transports exhibit a large degree of compensation: while the baroclinic flow tends to transport mass equatorward across SSH streamlines, the integrated barotropic transport is directed poleward. The total, the sum of baroclinic and barotropic cross-stream transport, is mostly determined by the larger barotropic component. Across the SAF the total cross-stream transport accumulates (becomes more negative) in a series of steps in the lee of the topographic obstacles. These are partially compensated by more positive transports across the center of the basins, and lead to circumpolar integral values of approximately −15 Sv across the three branches. The total transport across the northern and southern branches of the PF and the SACCF also becomes more negative due to the large negative values around the large topographic obstacles with a smaller contribution from the dynamics in the center of the basins. Approximately −5 Sv cross the SACCF, while −10 and −20 Sv cross the southern and northern branches of the PF. Ageostrophic transports, mainly due to Ekman flow, of equal magnitude and opposite sign exactly balance these geostrophic transports, leading to no net mass transport across the streamlines.

### 5.2. Contribution to the Temperature Transport Across the ACC

The contribution to the cross-stream heat transport by the time-mean geostrophic flow is often assumed to be small, consistent with equivalent barotropic flow. If the geostrophic flow is parallel to the surface flow at

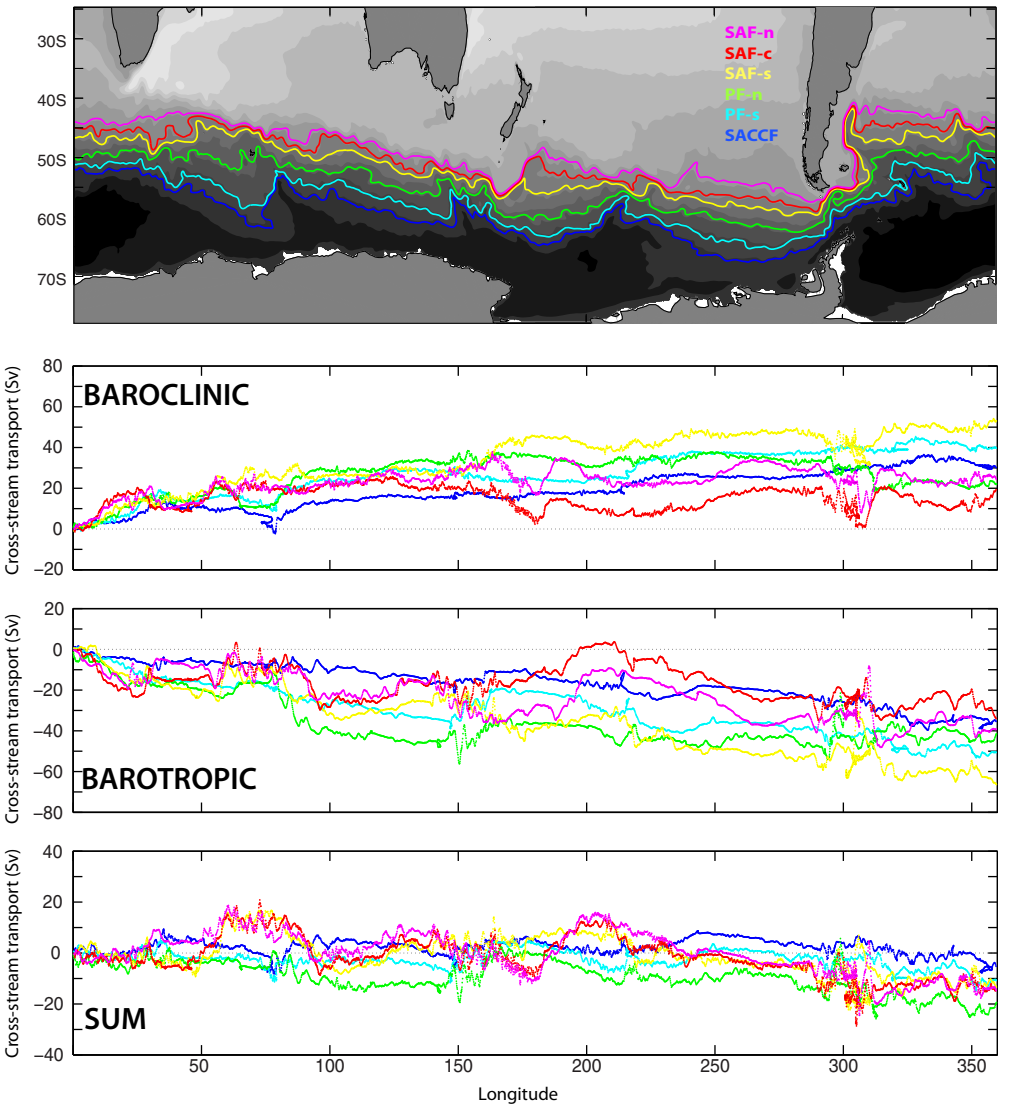


**Figure 10.** (top) Baroclinic, (middle) barotropic, and (bottom) sum cross-stream transports integrated along the SAF-n (purple), SAF-c (magenta), SAF-s (yellow), PF-n (green), PF-s (cyan), and SACCF (blue). The location of the fronts is shown in the SSH map atop. Note that the particular value of the integral at a given longitude depends on the origin of the integration.

all depths, then it is also parallel to the geostrophic shear and tangent to isopycnals. In the absence of a time-mean cross-stream flow other than Ekman transport near the surface, and with density largely determined by temperature at these latitudes, eddies are the main mechanism left to carry heat across the ACC below the Ekman layer. However, we have shown that in SOSE cross-stream volume transport by the time-mean geostrophic velocity is significant and will show next that temperature transport is significant as well.

Because temperatures in the upper ocean can be several times larger than the vertical average, variations in the vertical structure of the cross-stream flow could potentially be more significant in the heat transport than in volume transport. As the geostrophic flow alone, without the Ekman contribution, does not conserve mass, we calculate temperature rather than heat transport across SSH streamlines for the barotropic flow,

$$F_{BT} = \int_{s} \int_{-h}^{0} \hat{v}_{bot} T(z) \mathrm{d}z \mathrm{d}s'$$

and for the baroclinic flow,

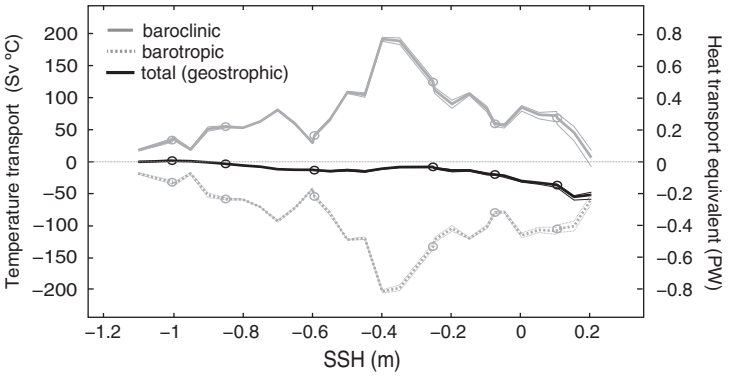


**Figure 11.** Cross-front temperature transport (left axis) and heat transport equivalent (right axis) by the time-mean geostrophic flow integrated along SSH streamlines in SOSE. The baroclinic component is shown in gray, barotropic in dashed gray, and the sum by the solid black line. The location of the values corresponding to the six frontal branches (see text for details) is indicated by the open circles along each of the curves. Standard errors for the transports estimated using the effective number of degrees of freedom are shown by the thin lines.

$$F_{BC} = \int_{s}\int_{-h}^{0} \hat{v}_{rel}(z)T(z)\mathrm{d}z\mathrm{d}s'$$

where as for volume transport $\hat{v}_{bot}$ and $\hat{v}_{rel}$ are the barotropic and baroclinic cross-stream velocity, $s$ is the along-stream direction, and now $T(z)$ is the time-mean temperature profile. The direction of the resulting temperature transport by the barotropic and baroclinic flow mirrors the direction of the volume transport (Figure 11), since the time-mean temperature is positive everywhere in the ACC. The baroclinic temperature transport (and heat equivalent) is positive everywhere; larger in the SSH range of the SAF with values around 125 Sv°C (0.5 PW), and rapidly decreasing toward the south. The barotropic temperature transport is poleward everywhere, with amplitudes slightly larger than the baroclinic component, and a similar pattern in amplitude. The resulting net geostrophic temperature transport is negative throughout the entire SSH range, with larger values toward the north, ranging between −25 and −50 Sv°C (−0.1 to −0.2 PW), and gradually tapering off to zero to the south. These temperature transports by the time-mean geostrophic flow are small compared to the temperature transports by the Ekman flow (equatorward) and transients (poleward), but comparable to the residual between Ekman and transients, hence an important component of the heat transport.

## 6. Discussion

The percentage of the zonal transport due to the barotropic component (defined as the near-bottom velocity times the water depth) is spatially variable. Barotropic transports integrated meridionally within the circumpolar ACC reach maximum values of 20% of the total transport over large topographic obstacles and constriction points such as northeast of the Kerguelen Plateau, at the Macquarie Ridge, through the Eltanin Fracture zone, over the Mid-Atlantic Ridge and at Drake Passage. These barotropic transports are larger than previously inferred values. In particular, at Drake Passage the whole transport of the ACC, the canonical 134 Sv estimated by *Whitworth and Peterson* [1985], was estimated to be carried by the baroclinic flow relative to the deepest common level [*Cunningham et al.*, 2003].

Locally, the percentage of the vertically integrated along-stream transport (with units of transport per unit length) carried by the barotropic component can reach values of 50% and higher in the vicinity of complex topography, both due to changes in vertical shear as well as enhanced near-bottom flows. Large bottom flows are a common feature to many models, as they are needed in order to transfer both the momentum [*Gille*, 1997] and vorticity [*Wells and De Cuevas*, 1995] input by the wind to the solid earth, which primarily happens at the large topographic obstacles. However, long term observations of the absolute time-mean velocity across the whole ACC do not exist, other than the various inferences at Drake Passage. At the regional level some observational evidence exists of enhanced barotropic flow around bathymetric features. On the North Scotia Ridge, based on data collected during a hydrographic survey, *Smith et al.* [2010] showed that the flow becomes more barotropic over the ridge, with 63% of the transport carried by the barotropic component (44 out of a total of 117 Sv was due to the shear component). A similar result was found at Macquarie Ridge from year-long current meter records by *Rintoul et al.* [2014], who found 80% of the transport was carried by the depth-independent component where the SAF passes through a gap in the ridge. Both reduced vertical shear and enhanced bottom velocities contributed to the strong barotropic

flow. Large bottom velocities and reduced vertical shear were also measured by *Sekma et al*. [2013] at Fawn Trough.

Following surface streamlines, vertical shear undergoes large top-to-bottom changes. In areas, where the flow is either constricted laterally or compressed vertically (e.g., Eltanin Fracture zone, Drake Passage, the Macquarie Ridge or Fawn Trough) surface velocities are larger and shear is enhanced, while in the center of the basins shear is in general reduced. Particularly large values of vertical shear are found in the Malvinas Current as well as through Fawn Trough in the Kerguelen Plateau. At both these locations, the ACC is vertically compressed and flows northward and upward adiabatically, to then return southward (and downward) along the rest of its circumpolar path with a rather different vertical structure. These changes in the vertical structure of the northward and southward flowing parts of the ACC are features of the time-mean circulation and can, without the need to invoke transient eddies, explain the *z*-space Southern Ocean Deacon Cell and its reduction when integrated along isopycnals, as pointed out by *Doos and Webb* [1994] and *Speer et al*. [2000].

Although shear anomalies are, in general, largest within the top 1500 m of the water column, they can extend all the way to the bottom and significantly contribute to the overall baroclinic structure of the ACC. Deep baroclinic effects are either not included at all or misrepresented in many of the available climatologies, which are often heavily based on observations from the upper 1000–2000 m of the ocean, and can, together with a poor representation of the barotropic component, explain the inferred lack of mass conservation when combined with existing mean dynamic topography products [*Griesel et al*., 2012].

Observations suggest that in the ACC the assumption of flow at depth being parallel to the surface flow breaks down at some locations along the current's path. *Chereskin et al*.'s [2009] direct velocity measurements as well as *Gille*'s [2003] inferences of bottom flows from the combined analysis of ALACE floats and hydrography have shown, like SOSE, that near-bottom velocities are not always aligned with the surface velocity field, thus the flow cannot be considered EB at these locations. In SOSE, mean velocity vectors in the upper 1500 m of the ACC remain within $\pm 10^{\circ}$ of the mean surface flow direction. Rotation increases with depth but remains relatively low in the deep part of the main jets. Larger angles are typically found in the jet flanks, and are often associated with elevated values of eddy kinetic energy. As shown by *Thompson and Naveira Garabato* [2014], enhanced deep eddy kinetic energy and large vertical velocities occur in the vicinity of standing meanders, where eddy-mean flow interactions are strong and likely to shape the patterns of rotation described here.

The enhanced turning of the velocity associated with stationary meanders results in large cross-stream transports. Along the northern edge of the Kerguelen Plateau and in the region between the Southeast Indian Ridge and the Macquarie Ridge, several tens of Sverdrups move across the fronts, alternating to the north and to the south over bands of a few degrees of longitude. In these regions, strain is large as a result of the interaction of the ACC with large topographic obstacles [*Naveira Garabato et al*., 2011], and the vorticity balance is that of short barotropic Rossby waves arrested by the mean flow [*Hughes*, 2005]. The presence of these lee-waves is supported by current observations south of Australia, which captured eastward propagating meanders occasionally stalling for several months [*Phillips and Rintoul*, 2000; *Tracey et al*., 2006]. Horizontal velocities measured by EM-APEX profiling floats near the Kerguelen Plateau show that rotation is large along meanders [*Phillips and Bindoff*, 2014].

Both barotropic and baroclinic flow contribute to the turning of the horizontal velocity with depth. The contribution from the barotropic component is dominant, and tends to oppose the sign of the baroclinic component; the baroclinic component, on average, carries mass across the fronts toward the equator, while the barotropic component carries mass toward the pole. In part, this is a consequence of the fact that, by construction, cross-SSH baroclinic velocity at the surface is exactly opposite to the barotropic velocity. Hence, even in the absence of rotation in the baroclinic flow, a baroclinic cross-stream transport occurs. The fraction of the baroclinic cross-stream transport due to rotation in the baroclinic flow varies along and across streamlines, ranging from 30 to 50% of the amplitude of the baroclinic cross-stream transport. Over the full path of the fronts, the sum of baroclinic and barotropic cross-stream transports is rather insensitive to the choice of streamline and carries approximately 5–20 Sv toward the pole across the SAF, PF, and SACCF. The majority of this transport happens at depth (below 2500 m), as rotation defined relative to the surface flow increases with increasing depth. These geostrophic transports are compensated by Ekman transports of equal magnitude and opposite direction.

The amplitude of the time-mean cross-stream velocities responsible for these transports is small ($<1$ cm $s^{-1}$) away from complex topography. In the vicinity of topographic obstacles, larger near-bottom flows at larger angles with the surface velocity translate into larger cross-stream velocities that range from a few to several cm $s^{-1}$. These flows are sufficiently large to be measured by present-day instrumentation. However, they vary over short spatial scales (O(100)km), thus measurements taken relatively short distances apart can lead to rather different results.

The lack of alignment between near-bottom and surface flow is to a large degree a consequence of potential vorticity conservation. In areas where meanders are typically found, the rotation of the deep flow has been linked to the presence of deep eddies spun up by the stretching of the lower-layer caused by the meanders [*Tracey et al*., 2006; *Chereskin et al*., 2009]. Their signature is evident in the large barotropic cross-stream transports that dominate the smaller scales. Vortex stretching induced by the large-scale gradual changes in the ocean depth manifests in the baroclinic component. In areas where the bottom shoals we find poleward baroclinic transports, whereas in areas where the bottom deepens baroclinic transports are directed equatorward. These patterns are consistent with a topographically induced $\beta$-spiral in which clockwise (counterclockwise) turning with increasing depth, here equivalent to poleward (equatorward) cross-front transport, is related to upwelling (downwelling).

Temperature transport across the time-mean surface streamlines in the ACC is similar in pattern to mass transport. The baroclinic component carries temperature northward while the barotropic temperature transport across all fronts is poleward. The sum of both components is poleward due to the slightly larger barotropic transports, and reaches $-0.2$ PW north of the SAF-n. *Sekma et al*. [2013] estimate 0.58 PW are carried poleward by the time-mean flow across the southern flank of the ACC by extrapolating values derived from moored current meter measurements at Fawn Trough. Like *Sekma et al*. [2013], we find that at Fawn Trough the flow rotates clockwise with increasing depth and locally temperature is transported poleward. However, over its whole path the SACCF and other SSH contours that pass through the area experience as much counterclockwise turning as they do clockwise, resulting in negligible temperature transport in the circumpolar integral. This illustrates the pitfalls of inference and extrapolation from localized measurements.

The cross-stream transports by the mean flow described here are a consequence of the turning of the velocity with depth, which is particularly large around topographic obstacles. Changes in the direction of the horizontal velocity with depth are often misrepresented or completely missing in reconstructions of the velocity field based on surface or integral properties such as the Gravest Empirical Mode (GEM). Cross-stream velocities derived from these type of products will mainly be in the form of transients and necessarily underestimate temperature and other property transports across the ACC. Reconstruction of the along-stream component by such methods on the other hand, can be more accurate, since the along-stream component is predominantly baroclinic and vertical shear of the along-stream flow is mainly a function of the surface velocity and SSH. Unlike GEM, which is purely baroclinic, other simplified models of the ACC based on the EB structure, include a barotropic component through referencing to the mean dynamic topography (MDT). However, inaccuracies in the available MDT products are large around complex topography [*Griesel et al*., 2012], where the barotropic mode is dominant and likely to be misrepresented. Maps such as those in Figures 4 and 5 can provide some guidance as to what areas in the Southern Ocean can be successfully monitored by methods that rely on the EB model.

## 7. Conclusions

Determining the absolute transport of the ACC was a challenge during the WOCE era, and continues to be so. Here we use a model of the Southern Ocean constrained by observations to characterize the contribution of barotropic and baroclinic geostrophic motions to the zonal, along-stream and across-stream transport in the time-mean ACC.

We find that the contribution from the barotropic flow to the time-mean zonal transport is spatially variable. On average it accounts for approximately 15% of total transport. This contribution can be of either sign, and although small in the center of the basins, it can be large near topography. Thus, monitoring the baroclinic component of the transport alone will underestimate the total transport in some areas, and overestimate it in others.

This variability in the partition between barotropic and baroclinic flow arises not only from changes in the near-bottom velocity, but from changes in the baroclinic flow. The spatial distribution of vertical shear

shows the baroclinic flow undergoes large changes in response to changes in topography. These are mainly of two types. First, in areas where the bottom is relatively shallow, the velocity profile is vertically compressed, which translates into large shear throughout the water column and often large near-bottom flows as well. And second, in areas where the flow is laterally constricted, the surface flow accelerates and the shear in the upper ocean increases (e.g., at the Mid-Pacific Ridge). The effect of lateral constriction on shear can be readily captured by simple EB models. Deep baroclinic changes, on the other hand, are not predictable based solely on knowledge of the surface flow.

As local observations have shown, we find that in general the time-mean geostrophic flow at depth is not aligned with the surface flow. Therefore, the flow in the ACC is not strictly EB. However, rotation tends to be weak in the jet centers, and these can be considered approximately EB. At depth and on the flanks of the jets, rotation is large. This non-EB flow associated with rotation can transport mass across streamlines. Both baroclinic and barotropic flow contribute to this cross-stream transport, and to a large degree they tend to compensate each other. Cross-stream baroclinic and barotropic flow are highly variable in space at a wide range of scales. Baroclinic cross-stream transports vary at the basin-scale and are driven by gradual rising and deepening of the seafloor. At scales of O(100 km), cross-stream transports are predominantly barotropic and caused by the large angles between surface and deep flow associated with stationary meanders in the lee of topographic obstacles. Although the mechanisms differ, rotation on both scales is connected to changes in topography. The barotropic contribution dominates the circumpolar integral, and leads to a poleward mass transport by the time-mean flow of up to $-20$ Sv, and a temperature transport equivalent to $-0.2$ PW, in contrast to the common assumption that the mean flow does not carry temperature across streamlines.

**Acknowledgments**

This work was supported by the Australian government's Cooperative Research Centres Program through the Antarctic Climate and Ecosystems Cooperative Research Centre (ACE CRC), and by the Australian Government Department of the Environment, the Bureau of Meteorology, and CSIRO through the Australian Climate Change Science Program. MRM acknowledges the National Science Foundation (NSF) for support of this research through grants OCE-1234473 and OPP-0961218. SOSE was produced using the Extreme Science and Engineering Discovery Environment (XSEDE), which is supported by National Science Foundation grant MCA06N007. The data used in this study can be found at sose.ucsd.edu. We would also like to thank the reviewers, specially Randy Watts, as their comments greatly improved the manuscript.

## References

Adcroft, A., C. Hill, and A. J. Marshall (1997), Representation of topography by shaved cells in a height coordinate ocean model, *Monthly Weather Rev.*, *125*(9), 2293–2315.

Bryden, H. L. (1976), Horizontal advection of temperature for low-frequency motions, *Deep Sea Res. Oceanogr. Abstr.*, *23*(12), 1165–1174.

Chereskin, T. K., K. A. Donohue, D. R. Watts, K. L. Tracey, Y. L. Firing, and A. L. Cutting (2009), Strong bottom currents and cyclogenesis in Drake Passage, *Geophys. Res. Lett.*, *36*, L23602, doi:10.1029/2009GL040940.

Cunningham, S. A., S. G. Alderson, and B. A. King (2003), Transport and variability of the Antarctic Circumpolar Current in Drake Passage, *J. Geophys. Res.*, *108*(C5), 8084, doi:10.1029/2001JC001147.

Donohue, K. A., E. Firing, and S. Chen (2001), Absolute geostrophic velocity within the Subantarctic Front in the pacific ocean, *J. Geophys. Res.*, *106*, 19,869–19,882, doi:10.1029/2000JC000293.

Doos, K., and D. J. Webb (1994), The Deacon Cell and the other meridional cells of the Southern Ocean, *J. Phys. Oceanogr.*, *24*, 429–442.

Dufour, C. O., J. Le Sommer, J. D. Zika, M. Gehlen, J. C. Orr, P. Mathiot, and B. Barnier (2012), Standing and transient eddies in the response of the Southern Ocean Meridional Overturning to the Southern Annular Mode, *J. Clim.*, *25*(20), 6958–6974.

Ferrari, R., and M. Nikurashin (2010), Suppression of eddy diffusivity across jets in the Southern Ocean, *J. Phys. Oceanogr.*, *40*, 1501–1519.

Ferrari, R., C. Provost, A. Renault, N. Sennéchael, N. Barré, Y.-H. Park, and J. H. Lee (2012), Circulation in Drake Passage revisited using new current time series and satellite altimetry. 1: The Yaghan basin, *J. Geophys. Res.*, *117*, C12024, doi:10.1029/2012JC008264.

Firing, Y. L., T. K. Chereskin, and M. R. Mazloff (2011), Vertical structure and transport of the Antarctic Circumpolar Current in Drake Passage from direct velocity observations, *J. Geophys. Res.*, *116*, C08015, doi:10.1029/2011JC006999.

Forget, G., B. Ferron, and H. Mercier (2008), Combining Argo profiles with a general circulation model in the north Atlantic. Part 1: Estimation of hydrographic and circulation anomalies from synthetic profiles, over a year, *Ocean Modell.*, *20*(1), 1–16.

Gille, S. T. (1997), The Southern Ocean momentum balance: Evidence for topographic effects from numerical model output and altimeter data, *J. Phys. Oceanogr.*, *27*, 2219–2232.

Gille, S. T. (2003), Float observations of the Southern Ocean. Part I: Estimating mean fields, bottom velocities, and topographic steering, *J. Phys. Oceanogr.*, *33*, 1167–1181.

Griesel, A., M. R. Mazloff, and S. T. Gille (2012), Mean dynamic topography in the Southern Ocean: Evaluating Antarctic Circumpolar Current transport, *J. Geophys. Res.*, *117*, C01020, doi:10.1029/2011JC007573.

Hughes, C. W. (2005), Nonlinear vorticity balance of the Antarctic Circumpolar Current, *J. Geophys. Res.*, *110*, C11008, doi:10.1029/2004JC002753.

Hughes, C. W., M. P. Meredith, and K. J. Heywood (1999), Wind-driven transport fluctuations through Drake Passage: A Southern Mode, *J. Phys. Oceanogr.*, *29*, 1971–1992.

Ivchenko, V. O., A. E. Krupitsky, V. M. Kamenkovich, and N. C. Wells (1999), Modeling the Antarctic Circumpolar Current: A comparison of FRAM and equivalent barotropic results, *J. Mar. Res.*, *57*, 29–45.

Karsten, R. H., and J. Marshall (2002), Testing theories of the vertical stratification of the ACC against observations, *Dyn. Atmos. Oceans*, *36*, 233–246.

Killworth, P. D. (1992), An equivalent-barotropic mode in the Fine Resolution Antarctic Model, *J. Phys. Oceanogr.*, *22*, 1379–1387.

Killworth, P. D., and C. W. Hughes (2002), The Antarctic Circumpolar Current as a free equivalent-barotropic jet, *J. Mar. Res.*, *60*, 19–45.

Krupitsky, A., V. M. Kamenkovich, N. Naik, and M. A. Cane (1996), A linear equivalent barotropic model of the Antarctic Circumpolar Current with realistic coastlines and bottom topography, *J. Phys. Oceanogr.*, *26*, 1803–1824.

Marshall, D. (1995), Topographic steering of the Antarctic Circumpolar Current, *J. Phys. Oceanogr.*, *25*, 1636–1650, doi:10.1175/1520-0485(1995)025.

Marshall, J., D. Olbers, H. Ross, and D. Wolf-Gladrow (1993), Potential vorticity constraints on the dynamics and hydrography of the Southern Ocean, *J. Phys. Oceanogr.*, *23*, 465–487.
Marshall, J., A. Adcroft, C. Hill, L. Perelman, and C. Heisey (1997), A finite-volume, incompressible Navier Stokes model for studies of the ocean on parallel computers, *J. Geophys. Res.*, *102*, 5753–5766, doi:10.1029/96JC02775.
Mazloff, M. R., P. Heimback, and C. Wunsch (2010), An eddy-permitting Southern Ocean State Estimate, *J. Phys. Oceanogr.*, *40*, 880–899.
Mazloff, M. R., R. Ferrari, and T. Schneider (2013), The force balance of the Southern Ocean Meridional Overturning Circulation, *J. Phys. Oceanogr.*, *43*(6), 1193–1208.
Meijers, A. J. S., N. L. Bindoff, and S. R. Rintoul (2011), Estimating the four-dimensional structure of the Southern Ocean using satellite altimetry, *J. Atmos. Oceanic Technol.*, *28*, 548–568, doi:10.1175/2010JTECHO790.1.
Moore, J. K., M. R. Abbott, and J. G. Richman (1999), Location and dynamics of the Antarctic Polar Front from satellite sea surface temperature data, *J. Geophys. Res.*, *104*, 3059–3073.
Munk, W. H., and E. Palmén (1951), Note on the dynamics of the Antarctic Circumpolar Current, *Tellus*, *3*, 53–55.
Nadeau, L-P., and D. N. Straub (2012), Influence of wind stress, wind stress curl, and bottom friction on the transport of a model Antarctic Circumpolar Current, *J. Phys. Oceanogr.*, *42*, 207–222.
Naveira Garabato, A. C., R. Ferrari, and K. L. Polzin (2011), Eddy stirring in the Southern Ocean, *J. Geophys. Res.*, *116*, C09019, doi:10.1029/2010JC006818.
Nikurashin, M., and R. Ferrari (2011), Global energy conversion rate from geostrophic flows into internal lee waves in the deep ocean, *Geophys. Res. Lett.*, *38*, L08610, doi:10.1029/2011GL046576.
Olbers, D., and C. Eden (2003), A simplified general circulation model for Baroclinic Ocean with topography. Part I: Theory, waves and wind-driven circulations, *J. Phys. Oceanogr.*, *33*, 2719–2737.
Olbers, D., D. Borowski, C. Vöelker, and J.-O. Wolff (2004), The dynamical balance, transport and circulation of the Antarctic Circumpolar Current, *Antarct. Sci.*, *16*(4), 439–470.
Orsi, A. H., T. Whitworth, and W. D. Nowlin (1995), On the meridional extent and fronts of the Antarctic Circumpolar Current, *Deep Sea Res., Part I*, *42*(5), 641–673.
Park, Y.-H., F. Vivier, F. Roquet, and E. Kestenare (2009), Direct observations of the ACC transport across the Kerguelen Plateau, *Geophys. Res. Lett.*, *36*, L18603, doi:10.1029/2009GL039617.
Phillips, H. E., and S. R. Rintoul (2000), Eddy variability and energetics from direct current measurements in the Antarctic Circumpolar Current south of Australia, *J. Phys. Oceanogr.*, *30*, 3050–3077.
Phillips, H. E., and S. R. Rintoul (2002), A mean synoptic view of the Subantarctic Front south of Australia, *J. Phys. Oceanogr.*, *32*, 1536–1553.
Phillips, H. E., and N. L. Bindoff (2014), On the non-equivalent barotropic structure of the Antarctic Circumpolar Current: An observational perspective, *J. Geophys. Res. Oceans*, *119*, 5221–5243, doi:10.1002/2013JC009516.
Rhines, P. (1970), Edge-, bottom-, and Rossby waves in a rotating stratified fluid, *Geophys. Fluid Dyn.*, *1*, 273–302.
Rintoul, S. R., and S. Sokolov (2001), Baroclinic transport variability of the Antarctic Circumpolar Current south of Australia (woce repeat section sr3), *J. Geophys. Res.*, *106*, 2815–2832, doi:10.1029/2000JC900107.
Rintoul, S. R., S. Sokolov, M. J. M. Williams, B. Peña Molino, M. Rosenberg, and N. L. Bindoff (2014), Antarctic Circumpolar Current transport and barotropic transition at Macquarie Ridge, *Geophys. Res. Lett.*, doi:10.1002/2014GL061880, in press.
Roquet, F., Y.-H. Park, C. Guinet, F. Bailleul, and J.-B. Charrassin (2009), Observations of the Fawn Trough current over the Kerguelen Plateau from instrumented elephant seals, *J. Mar. Syst.*, *78*, 377–393.
Sekma, H., Y.-H. Park, and F. Vivier (2013), Time-mean flow as the prevailing contribution to the poleward heat flux across the southern flank of the Antarctic Circumpolar Current: A case study in the Fawn Trough, Kerguelen Plateau, *J. Phys. Oceanogr.*, *43*(3), 583–601.
Smith, I. J., D. P. Stevens, K. J. Heywood, and M. P. Meredith (2010), The flow of the Antarctic Circumpolar Current over the North Scotia Ridge, *Deep Sea Res., Part I*, *57*, 14–28, doi:10.1016/j.dsr.2009.10.010.
Sokolov, S., and S. R. Rintoul (2007), Multiple jets of the Antarctic Circumpolar Current south of Australia, *J. Phys. Oceanogr.*, *37*, 1394–1412.
Sokolov, S., and S. R. Rintoul (2009), Circumpolar structure and distribution of the Antarctic Circumpolar Current fronts. 1: Mean circumpolar paths, *J. Geophys. Res.*, *114*, C11018, doi:10.1029/2008JC005108.
Speer, K., S. R. Rintoul, and B. Sloyan (2000), The Diabatic Deacon cell, *J. Phys. Oceanogr.*, *30*(12), 3212–3222.
Sun, C., and D. R. Watts (2001), A circumpolar gravest empirical mode for the Southern Ocean hydrography, *J. Geophys. Res.*, *106*, 2833–2855, doi:10.1029/2000JC900112.
Swart, S., S. Speich, I. J. Ansorge, G. J. Goni, S. Gladyshev, and J. R. Lutjeharms (2008), Transport and variability of the Antarctic Circumpolar Current south of Africa, *J. Geophys. Res.*, *113*, C09014, doi:10.1029/2007JC004223.
Thompson, A. F. (2010), Jet formation and evolution in baroclinic turbulence with simple topography, *J. Phys. Oceanogr.*, *40*, 257–278.
Thompson, A. F., and J.-B. Sallée (2012), Jets and topography: Jet transitions and the impact on transport in the Antarctic Circumpolar Current, *J. Phys. Oceanogr.*, *42*(6), 956–972.
Thompson, A. F., and A. C. Naveira Garabato (2014), Equilibration of the Antarctic circumpolar current by standing meanders, *J. Phys. Oceanogr.*, *44*, 1811–1828.
Tracey, K., D. Watts, C. Meinen, and D. Luther (2006), Synoptic maps of temperature and velocity within the Subantarctic Front south of Australia, *J. Geophys. Res.*, *111*, C10016, doi:10.1029/2005JC002905.
Viebahn, J., and C. Eden (2012), Standing eddies in the Meridional Overturning Circulation, *J. Phys. Oceanogr.*, *42*, 1486–1508.
Wells, N., and B. De Cuevas (1995), Depth-integrated vorticity budget of the southern ocean from a general circulation model, *J. Phys. Oceanogr.*, *25*(11), 2569–2582.
Whitworth, T., III, and R. Peterson (1985), Volume transport of the Antarctic Circumpolar Current from bottom pressure measurements, *J. Phys. Oceanogr.*, *15*(6), 810–816.
Zika, J. D., et al. (2013), Vertical eddy fluxes in the Southern Ocean, *J. Phys. Oceanogr.*, *43*(5), 41–955.